Soft Matter

PAPER

View Article Online
View Journal | View Issue

Cite this: *Soft Matter*, 2026, **22**, 1416

Local cargo delivery to double bilayer compartments

Rui Liu, †[a] Ruslan Ryskulov,†[a] Esteban Pedrueza-Villalmanzo,[a] Irep Gözen[b] and Aldo Jesorka*[ab]

Received 26th September 2025,
Accepted 9th January 2026

DOI: 10.1039/d5sm00978b

rsc.li/soft-matter-journal

In this work we investigated the encapsulation of fluorescent cargo during temperature-induced formation of lipid double bilayer membrane pockets on silicon carbide substrates. This exotic mode of autonomous membrane transformation, so far only observed on silicon carbide, leads to double-bilayer-enveloped compartments. For localized superfusion and investigation of cargo transfer to the emerging pockets, a hard polymer (photo-crosslinked SUEX™ epoxy) open space microfluidic device was developed. Encapsulation occurs rapidly, and cargo is effectively retained in pockets between distal and proximal bilayer, but escapes de-wetted compartments through double bilayer ruptures that connect the compartment interior to the surrounding medium.

1. Introduction

Interaction between various high-energy surfaces and lipid membranes received significant attention with respect to membrane rupture, membrane repair and topological transformations.[1–3] Models were suggested in conjunction with new origin of life hypotheses suggesting the possible involvement of solid surfaces in the development of prebiotic primitive cells.[4–6] Surface energy causes conversion of flat giant unilamellar vesicles (FGUV), *i.e.*, double bilayers autonomously formed from surface-deposited multilamellar vesicles (MLVs), into compartments and nanotube networks.[7–9] We have recently reported a double lipid bilayer (DLB) transformation regime leading to complete de-wetting[10] of silicon carbide (SiC) substrates under formation of membrane-enclosed compartments with contact of the internal contents to the surface. This particular transformation was initiated by local temperature increase.[11–13] We observed different rupture modes of affected membrane patches, followed by the formation of pockets and superstructures, similar in structure to the systems described by Katke *et al.*[14] Membrane pockets with de-wetted surface underneath are of interest in the origin of life context, since access of internalized cargo to the surface creates possibilities for catalytic interactions and exchange of material.[15–18] A key question remaining was whether external solution becomes encapsulated in newly formed compartment in this de-wetting process, which was shown to occur in related structures on other engineered and natural surfaces.[13,14] SiC is foremost an engineering material, but is also found in the natural mineral Moissanite, and as presolar grains in meteorites and interstellar dust.[19]

By combining microfluidic superfusion with IR-heat stimulation of double bilayer membrane patches on silicon carbide substrates, we have now investigated the uptake of water-soluble small fluorophore molecules by the arising membrane compartments and their ability to retain the cargo (Fig. 1). For that purpose, a microfluidic solution delivery system, comprising an open space microfluidic device for localized solution delivery was fabricated. Its microfluidic chip is functionally related to our multifunctional pipette, earlier developed for superfusion of adherent tissue cultures and surface-integrated sensors. Open space microfluidics offers the ability to sequentially deliver nanoliter fluid volumes gently to selected surface areas in a fluid sample, while leaving structures in other regions unaffected.[20–22] The original device, fabricated in poly(dimethyl siloxane) (PDMS) elastomer by a soft replica technology, has shown its utility in microscopy-dependent experimental environments.[23–26] Unfortunately, it has frustrating drawbacks with respect to solvent resistance, cleanroom compatibility of the fabrication process and production upscaling. For microscopy applications, the large footprint of the original device is particularly problematic during application, since positioning can be cumbersome as the device causes shadows in the field of view under an inverted microscope.

We achieved an improvement by fabricating a hard polymer variant of the device with a footprint close to the channel size. This initial approach, having yielded a functional prototype device, was promising but also associated with intrinsic fabrication-related obstacles.[27] We therefore proceeded to utilize SUEX negative dry-film photoresist. The use of this material

[a] *Department of Chemistry and Chemical Engineering, Chalmers University of Technology, 41296, Göteborg, Sweden. E-mail: aldo.jesorka@gomod.eu*
[b] *GOMOD AB, Göteborg, Sweden*
† These authors contributed equally to this work.

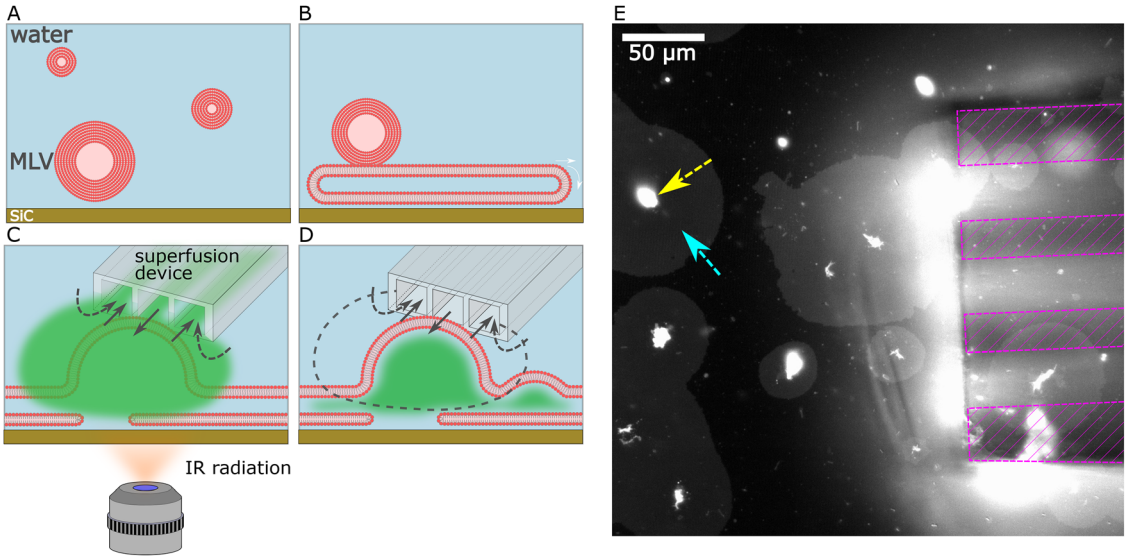

Fig. 1 Heating/superfusion-enabled loading of double bilayer membrane compartments. (A) Deposition of MLVs from the lipid suspension onto SiC surfaces in buffer solution. (B) MLV spreading under double bilayer membrane patch formation by a tank-tread motion, *i.e.* spreading from the MLV reservoir of low membrane tension towards the edge region of high tension. (C) Double bilayer de-wetting and pocket formation on the lipid double bilayer membrane, while simultaneously heating and locally superfusing with a fluorophore solution. Gray arrows denote the flow of fluid in and out of the device, forming a hydrodynamically confined volume inside the sample. (D) Membrane pockets with retained fluorophore solution after flow switching in the microfluidic device to non-fluorescent buffer (gray dashed line). Panels A–D are schematic, not to scale. (E) Micrograph showing the sample region with spreading lipid patches on SiC approached by the pipette tip prior to superfusion (panel D). Device outline and channel borders are highlighted with magenta dashed lines. The yellow arrow points to one of the MLV lipid reservoirs, the blue arrow to the corresponding spreading patch.

for microdevice fabrication has been reported in various applications in recent years, including microwave applications, soft-replica master production and closed-channel microfluidic devices.[28–30] Processing of SUEX dry resist involves layer-by-layer lamination in combination with photolithography, and circumvents the requirement for handling liquid resist formulations, spin-coating and long wafer rest periods for layer height equilibration, which is of concern when up-scaling to larger wafer sizes is considered. The hard polymer microdevices produced from dry film are of sub-millimeter thickness with a small footprint and optically transparent.[31] The process was subsequently improved to produce simple open space microfluidic devices with small channel sizes <50 μm, using a specially prepared carrier wafer.[32]

For practical superfusion applications of this device type, a sharp needle-like tip is desirable, as it facilitates wetting of the material upon entry into the open volume and makes positioning in an inverted light microscope setup particularly easy. Our initial dry film fabrication attempts of sharp-tipped devices revealed persistent problems related to unwanted deformation of the film during lamination, which made the devices unusable. We therefore report here a new design concept, according to which we successfully produced optically transparent, needle-shaped superfusion chips in epoxy polymer comprising the internal flow-steering circuitry earlier developed in our laboratory.[27] These devices were used to expose double bilayer membrane patches on SiC substrates in a laser microscopy setup, combining imaging and a IR-B laser source for heating through the objective. Encapsulation of fluorophore cargo (Alexa Fluor 633) delivered by the device was monitored and characterized (Fig. 1).

2. Materials and methods

Chemicals and solvents

Solvents, reagents, buffer components are HPLC grade or of higher purity. Buffer components were dissolved in de-ionized water (MilliQ, 18.2 MΩ). Alexa Fluor 633 (ThermoFisher) was used for superfusion experiments. The solution was prepared in DMSO according to the manufacturer's specifications.

Lipid preparation reagents

Soybean polar lipid extract (SPE, Avanti Polar Lipids), E.coli polar lipid extract (Avanti Polar Lipids), 1,2-dipalmitoyl-*sn*-glycero-3-phosphoethanolamine-*N*-(lissamine rhodamine B sulfonyl) (ammonium salt) (16 : 0 Liss Rhod PE), Avanti Polar Lipids), glycerol (Sigma-Aldrich), chloroform (Sigma-Aldrich).

Buffer solution components

Trizma base (Sigma-Aldrich), potassium hydrogen phosphate (98%; K_2HPO_4, Sigma-Aldrich), potassium dihydrogen phosphate (KH_2PO_4, Sigma-Aldrich), magnesium sulfate ($MgSO_4 \cdot 7H_2O$, Sigma-Aldrich), Na_2EDTA (Fluka). Aqueous buffer solvents were pH-adjusted with reagents: phosphoric acid (H_3PO_4, Sigma-Aldrich), sodium hydroxide (NaOH, Sigma-Aldrich).

Preparation of lipid vesicle suspension

Lipid vesicle suspensions were prepared following the dehydration–rehydration method described earlier.[10,11] The above-mentioned lipid species (*E. coli* polar extract: Soy-bean polar extract, 49:50 wt%) and lipid-conjugated fluorophore (Rhodamine

PE, 1 wt%) were dissolved in chloroform, leading to a final concentration of 10 mg mL^{-1}. 300 μL of this solution was transferred to a 10 mL round bottom flask and the solvent was removed in a rotary evaporator at reduced pressure (20 kPa) for 6 hours to form a dry lipid film. The film was rehydrated with 2970 μL of PBS buffer and 30 μL of glycerol, and stored at +4 °C overnight to allow swelling of the lipid layers. The flask was sonicated next day for 25 s at room temperature, leading to the lipid suspension containing giant uni- and multilamellar compartments. The final lipid suspension was aliquoted to 20 μL tubes and stored at −20 °C. Before each microscopy experiment, 4 μL of this lipid suspension was desiccated for 20 min; then the dry residue was rehydrated with 0.5 mL of PBS buffer. Rehydrated suspension was transfered to a sample dish (Ø 47 mm, WillCo Wells, The Netherlands) with a glass bottom coated with SiC. All experiments were performed in an aqueous reservoir.

Fabrication of SiC surfaces

SiC surfaces were produced by thin layer deposition as described previously.[10]

Imaging

A Leica DM-IRB2 inverted microscope in a wide field laser induced fluorescence setup was used for the imaging of the lipid membrane patches.[10,11] A 10x objective with a 0.40 numerical aperture (NA) was used for obtaining the images in Fig. 2C and D; 20× (water) NA 0.75 for the imaging for Fig. 1E; 100× (oil) NA 1.40 for the imaging for Fig. 3 and 4 and Fig. S3–S8. Fluorescent label Liss rhod PE was excited at 532 nm with a diode laser (240 mW, Cobolt 06-MLD, Hubner Photonics, Germany), Alexa Fluor 633, used as cargo for the vesicle superfusion, was excited at 640 nm (MRL-III-640-150 mW, PhotonTec Berlin GmbH), the emitted light was imaged using a digital camera (Prosilica GX, Allied Vision Technologies, Germany).

Laser heating

Heat transformation of the lipid membrane was accomplished with an infrared B-band (IR-B) laser (1470 nm, 3.7 W, 4PN-104, Seminex, USA), coupled into the optical imaging setup.[10,11]

Image processing

Bright field and fluorescence images were analysed with the ImageJ/Fiji software package (National Institutes of Health, USA). Raw micrographs were adjusted for the figures for brightness and contrast. Intensity profiles for Fig. 3C, H, Fig. 4A, I, J and Fig. S5A, I, Fig. S8A, J were plotted with the OriginLab software package.

Device operation

The pipette tips were taped with double sided transfer tape (Type 467 MPF, 3M) onto a 3D-printed holding frame with integrated solution reservoirs, and mounted to an electronic micromanipulator (PatchStar, Scientifica). An in-house developed multichannel pneumatic pressure source was used to drive the fluids. Pressure values for operation with an outflow/inflow ratio $q \sim 0.75$ were set as follows:

Drive pressure active solution $P1$ = 150 mbar,
Standby pressure inactive solutions $P2$ = 10 mbar,
Recirculation vacuum $V1$ = −60 mbar,
Flow steering vacuum $V2$ = −40 mbar.

Fluorophores and buffers

Fluorescent solutions were utilized to examine the function of the switching chamber and recirculation area of the microfluidic device (Fig. 2C and D), and to determine the pressure parameters for operation. The water-soluble fluorescent dyes: 1% Rhodamine B (Sigma-Aldrich) in water as solution 1 and 1% fluorescein in water (Sigma-Aldrich) as solution 2 were used. Solution 3 was pure water.

Fabrication of the multifunctional micropipette

Devices (Fig. 2A) were produced in a newly developed negative dry film photoresist using mask photolithography in combination with multilayer roll lamination.[32] This originally reported process was optimized for high-yield fabrication of the needle-shaped device at the design level (*cf.* Fig. S1).

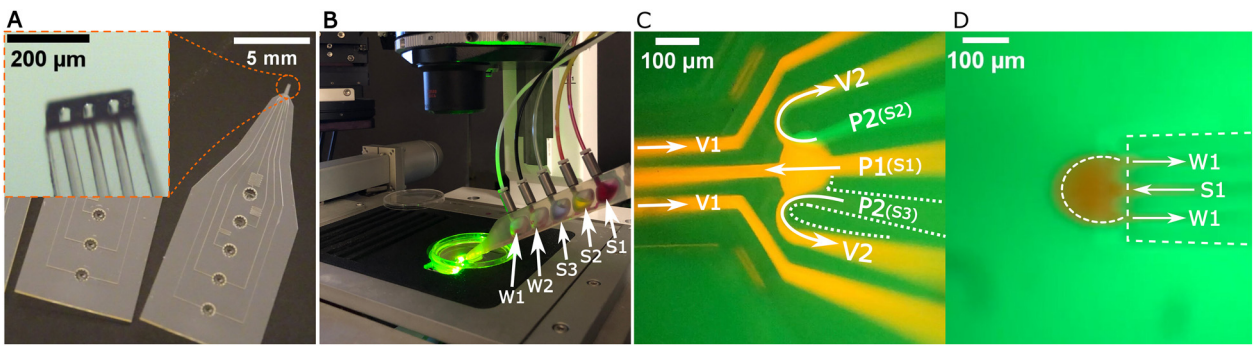

Fig. 2 SUEX-laminated microfluidic device fabricated for the superfusion experiments. (A) Photograph of the wafer scale-fabricated microfluidic pipette. The inset shows a magnification of the tip region with channel exits, obtained under an optical microscope at 5× magnification. (B) General view on the assembled setup during an encapsulation experiment: W1-2 denotes reservoirs for aspirated waste, S1-3 supplied individual solutions for superfusion. S1: fluorophore 1, S2: fluorophore 2, S3: aqueous buffer. (C) Micrograph showing design and function of the flow switching chamber. Buffer and fluorescent solution are applied. The four pressure sources (vacuum $V1$ and $V2$ and positive pressures $P1$ and $P2$) as well as connections to solution reservoirs S1–S3 are denoted in the image (*cf.* Section S2). (D) Fluorescence micrograph of the fluid recirculation area at the tip of the pipette in an open volume.

Mounting and deployment of the microfluidic device

Double-sided transfer tape was prepared according to the device outline, using a cutting plotter (Cricut Inc.). The tape was deposited onto a 3D printed manifold (Formlabs resin printer Form3B+), containing solution reservoirs and pressure connectors. Subsequently, the device was attached to the holder and mounted to a microscope-attached electronic micromanipulator[32] (Section S2).

Device characterization

A device was sacrificed to determine the flow performance. Proper device function was confirmed by means of fluorescent dye solutions. The channel size-dependent flow control parameters: active and passive inlet pressures, recirculation and flow control vacuum values (Fig. 2C and D) were in good agreement with previously determined values.[20] Fig. 2C shows a micrograph of the switching circuit set to inject solution 1. Fig. 2D is a fluorescence micrograph of the hydrodynamic solution confinement (solution recirculation zone) in an open volume consisting of water, where the outflow/inflow ratio was $q \sim 0.75$.

3. Results and discussion

Heat influenced membrane transformation on SiC surface

As reported in the earlier work[10] on SiC substrates, lipid membrane patches rupture and undergo at elevated temperatures a transformation to form double bilayer pockets with de-wetting of the surface within the pockets. The effect is highly localized and leaves surrounding membrane areas unaffected.[10,11,33] We earlier analyzed the locality of IR-B laser through-objective spot heating. A thermoresponsive polymer solution (the lower critical solution temperature polymer poly (*N*-isopropyl acrylamide)) was subjected to spot heating and the temperature gradient across its effective distance was determined *via* imaging of the coil to globule transition of the polymer at different laser powers.[33] Exposing selected patches (Fig. 3A and F) locally to a fluorophore solution (Alexa Fluor 633) by means of the microfluidic superfusion device, transfer of the fluorophore into the membrane pockets could be followed and characterized. We chose the water soluble fluorophore Alexa Fluor 633 as cargo molecule due to its photostability, its minimal interaction with lipid membranes and compatibility with our two color imaging setup. Two monitored regions and associated analysis results are displayed in Fig. 3B–D and G–I. The morphology of the patches was visualized with a membrane-attached fluorophore (Rhodamine PE), such that the membrane transformations could be followed. The superfusion device was in operation but is not visible in these panels. Panels C and H contain the related fluorescence intensity analysis results for the vectors overlaying panels B and G, which confirm the formation of double bilayer pockets. Differences in the layer structure of the pockets were observed in agreement with the earlier reported observations.[10] Some pockets are open to the de-wetted SiC surface, *i.e.*, both distal (upper) and proximal (lower with respect to the substrate) bilayer detached from the substrate. This situation is dominant in the first image series A–E, whereas the second image series F–J shows regions that are mainly fully membrane enclosed: only the distal bilayer detached to form pockets. The mechanism of compartmentalization by distal bilayer de-wetting has been reported earlier[13,14] and is here not discussed further.

The intensity profiles of lipid membrane patches in panels B and G reveal information about the membrane structures. Profiles I, II and III (panel C) indicate complete de-wetting of the surface from the double bilayer.Yellow arrows indicate a DLB with respect to the substrate. The surface under the pockets was identified as intensity minima (red arrows) between two oversaturated intensity profile spikes originating from the pocket boundaries. This minima are equal in intensity to a DLB, and indicates direct exposure of the pockets' internal volume to the substrate.[10] Similarly, the minimum under the pocket on profile III in panel C, (blue arrow) is an isolated compartment that is separated from the substrate by a second DLB. The membrane patch in panel G with the correspondent intensity profiles IV and V (H) show exclusive distal bilayer de-wetting, leading to pocket formation. The intensity profile shows no minima at the surface level, pocket minima (denoted by red arrows) are situated on single lipid bilayer (SLB) 1. Accordingly, the pockets feature no surface contact and can be seen as isolated structures similar to surface-adhered giant unilamellar vesicles. For comparison, remaining DLB regions on the ruptured patch are denoted by yellow arrows.

For both experiments, the cargo fluorophore emission channels are displayed alongside their overlays with the membrane fluorophore (Rhodamine PE) emission channel. Some of the transformed membrane patches have captured and encapsulated a fraction of the delivered fluorescent material (panels D, E and I, J). Further examples are supplied in Fig. S3–S8.

The two cases represented by the two image series show differences with respect to the location of the encapsulated cargo, and consequently its fate, which we relate to the presence of a direct connection of the pockets *via* de-wetted, *i.e.* fractured, areas to the surface. The encapsulation in de-wetted membrane pockets (first image series, panels A–E) is temporary, encapsulated material rapidly escapes, indicating that the de-wetted regions under the pockets have a connection with the exterior volume. The nature of these fractures spanning both bilayers and connecting the interior and exterior through channels had been discussed in our previous report.[10]

In contrast, cargo fluorophore in the fully membrane-enclosed pockets are preserved for much longer periods of time. The encapsulated fluorophore is apparently confined in between the proximal and distal bilayer, where a connection to the network of fractures beneath the patches is not established. This encapsulation mode can in the first case, where the pockets themselves do not retain fluorophore (Alexa Fluor 633), also be observed between the two bilayers around some of the pockets (panels D and E). The distal bilayer forms a superstructure above the pockets formed by the proximal bilayer.

Retention of cargo in membrane pockets

The residence time for the fluorescent material encapsulated by the membrane pockets on the patches showing complete DLB

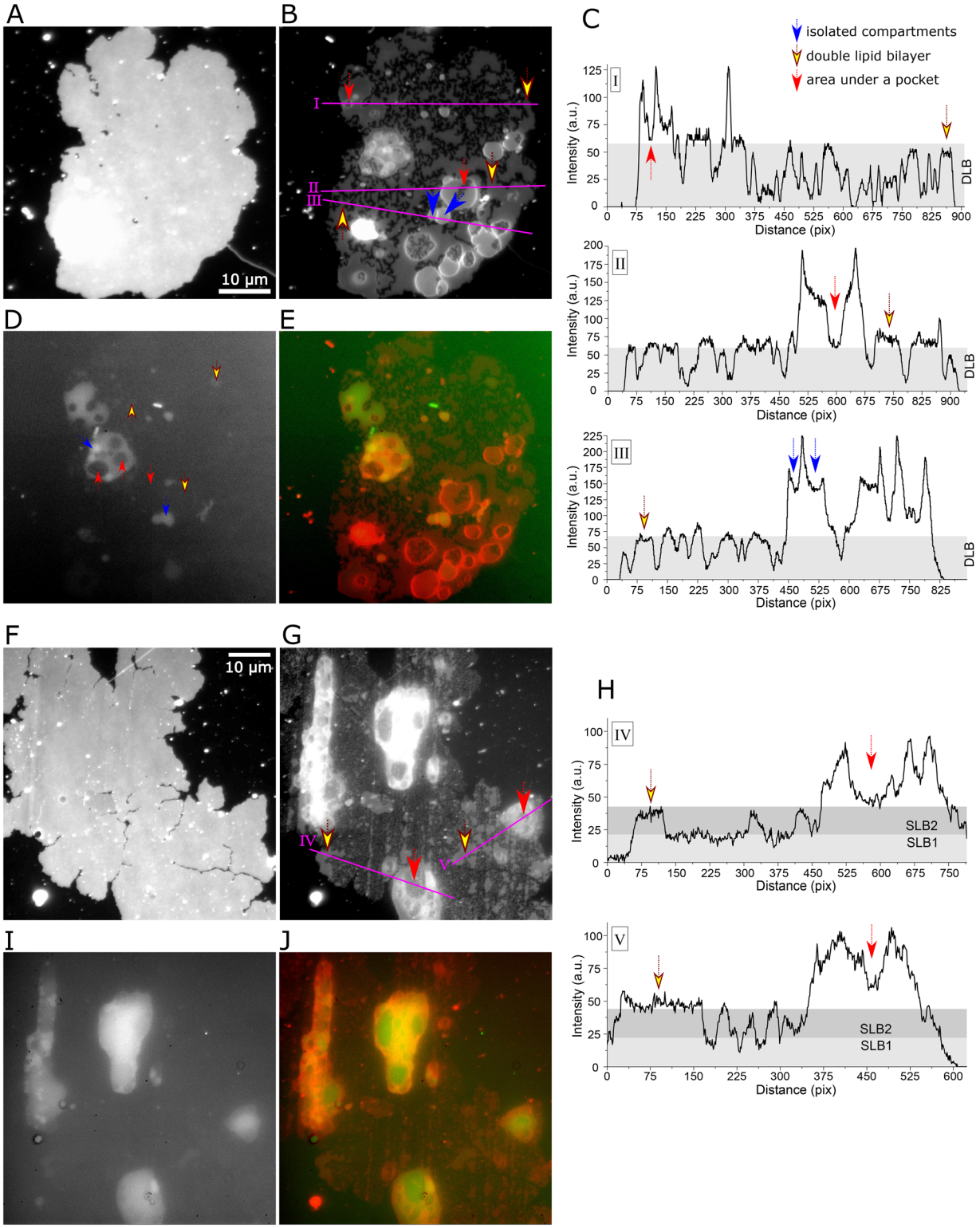

Fig. 3 Heat-induced transformations of double lipid bilayer membrane patches. (A) Double bilayer patch #1 on a SiC substrate before transformation. The membrane is stained with a lipid-conjugated fluorophore (Rhodamine B). (B) De-wetting of membrane patch shown in (A), magenta lines I, II and III correspond to intensity profiles in (C). The intensity values (arbitrary units, a.u.) on the *y*-axis are derived from the gray scale values of the images (Min:0-Max:255). (D) Fluorescence channel of encapsulated fluorophore solution (Alexa Fluor 633). (E) Merged fluorescence channels combining panels B and D. (F) Double bilayer patch #2 before transformation. (G) De-wetting of surface region in panel F, where magenta lines IV, V correspond to intensity profiles shown in panel H. (I) and (J) show cargo fluorescence channel and overlay with membrane channel G, respectively.

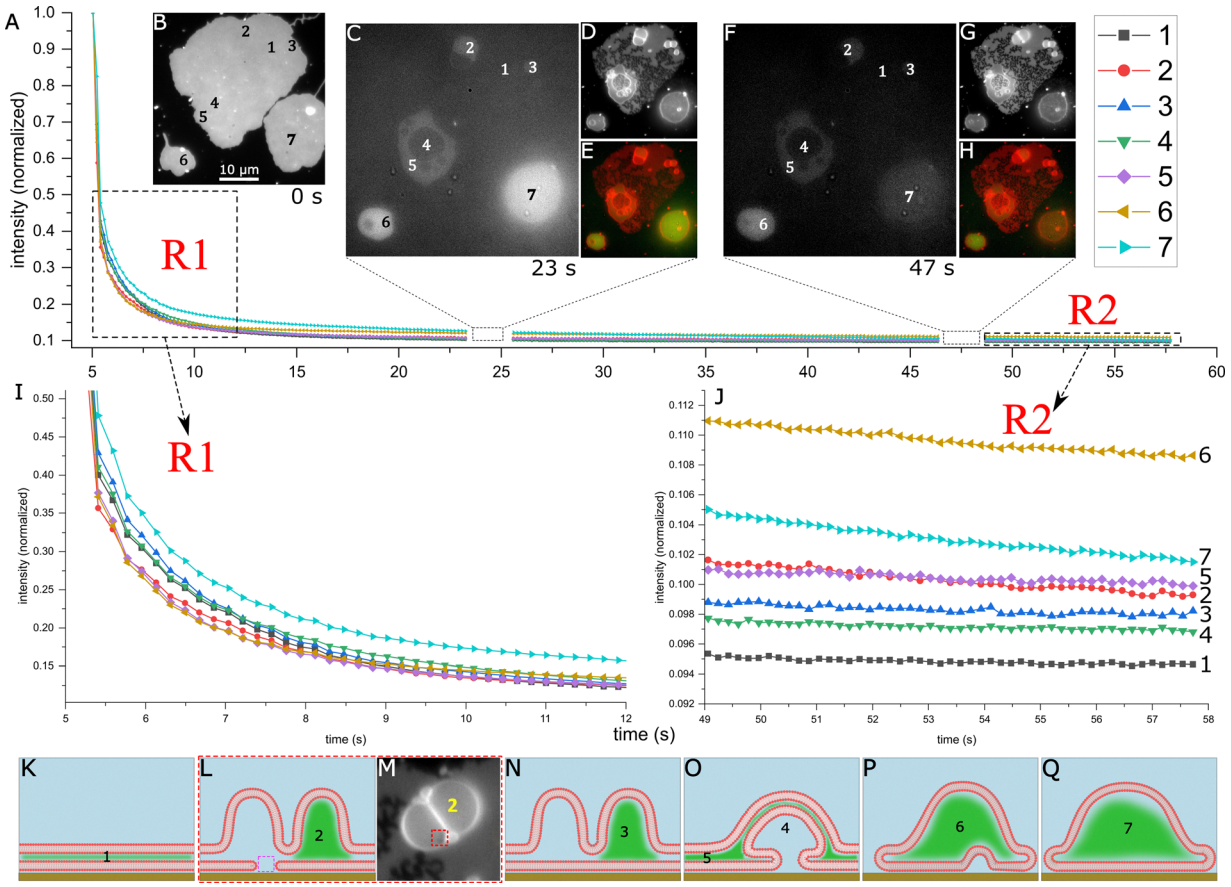

Fig. 4 Time development of cargo fluorescence in different areas on transformed membrane patches. (A) Development of fluorescence intensity over time in seven regions after heat-induced shape transformation under encapsulation of externally supplied fluorescent Alexa Fluor 633 dye solution. Panels B–H, arranged as insets to panel A, are micrograph sets taken at different time points: 0 s, 23 s and 47 s after transformation/superfusion; (B) (0 s): Double bilayer patches on a SiC substrate before transformation; (C)–(E) (23 s): (C) Fluorescence channel of encapsulated fluorophore solution (Alexa Fluor 633), (D) membrane label fluorescence channel, (E) merged channels combining (C) and (D); (F)–(H) (47 s): (F) Fluorescence channel of encapsulated fluorophore solution (Alexa Fluor 633), (G) membrane label fluorescence channel, (H) Merged channels combining (F) and (G). (I) and (J): magnified regions R1 and R2 of the decay graphs shown in panel A. (K)–(Q): Schematic drawings of encapsulation scenarios according to the images with area designations shown in panels B–H. Panel M shows a detail of panel D (fluorescence micrograph of the membrane channel) in conjunction with panel L. The internal rupture is marked with a red frame in both panels. Note that the gaps in the intensity decay graphs in A correspond to the short time intervals when snapshots of the membrane were captured (insets D and G). The imaging system is limited to one laser line at a time.

de-wetting was further investigated. The fluorescence decay diagram in Fig. 4A shows a timeline of the detectable presence of fluorescence signal in selected patch areas after heat-induced transformation and superfusion. Three adjacent patches (Fig. 4B) underwent de-wetting. We observe a rapid drop in fluorescent signal shortly after the microfluidic device was switched from fluorescent to non-fluorescent buffer solution (magnified region R1). Photobleaching is certainly responsible for a share of the decrease in fluorescence intensity over time. However, we do not think that photobleaching is the key factor in the drop of the intensity in the monitored regions of interest. The flip in the cargo fluorescence intensity levels between ROI #6 and #7 as well as ROI #2 and #5 over time supports that different membrane structures have different leakage behavior, possibly owing to the presence of transient pores.[13] Initially, fluorescent cargo was taken in by several membrane structures (Fig. 4C–E, representing cargo fluorescence, membrane fluorescence and overlay channels). We noticed that some compartments retained the cargo solution, while others quickly lost their contents. After 20 s, the remaining content was compared to the initial situation (F–H). Seven different patch areas, denoted with 1–7 in panels C and F were selected and analysed with respect to residual cargo content by comparing their fluorescence decay graphs. Magnifications of regions R1 and R2 in the fluorescence decay graphs are shown in Fig. 4I and J and are related to the structure and location of patch areas 1–7. The areas 1–5 belong to the same lipid patch, while 6 and 7 are originating from different individual patches. The largest lipid patch with areas 1–5 underwent complete de-wetting with numerous ruptures, area 6 shows a single de-wetted surface spot within a pocket spanning the entire patch, and area 7 shows an unruptured patch with cargo encapsulated between proximal and distal bilayer. The areas have associated representations in the intensity charts in the magnified region R2 of Fig. 4J. The recorded differences in retention of cargo can be interpreted by considering the structures of the pockets and membrane arrangements in the

different patch areas, as suggested in the schematic drawings in Fig. 4K–Q. The double bilayer structure, *i.e.* a section of an FGUV as shown in Fig. 4K, represents the lipid patches prior to transformation (area 1). It is abundantly present in the patch surrounding areas 2–5. Very little cargo is encapsulated within these membranes. A possible mechanism of encapsulation through transient pores has been discussed earlier. The membrane tension is known to increase with temperature increase, which facilitates the formation of such pores in our system.[13] Area 2, represented by Fig. 4L, shows a closed pocket with intact proximal bilayer in the vicinity of a pocket with de-wetted internal surface. The effectively closed pocket is surrounded by the FGUV structure (*cf.* panel K). An FGUV can be viewed as a nanofluidic system, in which diffusive exchange is slow. Pocket (2) in panel L retains the cargo and is only slowly being depleted. Panel M is a magnified fluorescence micrograph (membrane-labelled) of such a pocket. The situation is similar for area 3, designating the pocket depicted in panel N. Cargo is also retained in this structure; there appears to be no difference between being located next to a container with or without proximal bilayer rupture. The corresponding decay graphs of areas 2 and 3 in Fig. 4 are located close to each other. Area 4 is surrounded by area 5, it features completely de-wetted surface and can therefore be considered directly connected *via* the membrane ruptures to the outside environment. Its remaining fluorescence intensity is distinctly smaller than that of area 5 (panel O), which is clearly visible even in the fluorescence micrographs. Likely, the encapsulated material rapidly escapes though the fractures underneath the pockets. Areas 6 and 7, represented by panels P and Q, show remarkable differences. They are closed structures of distal bilayers without access to de-wetted surface. They feature the highest amounts of remaining cargo, particularly region 6 (*cf.* corresponding graphs in panel J). This is likely due to the absence of ruptured membrane around the structures, here the entire original patches have been transformed into giant vesicles, with area 6 being a superstructure enveloping a pocket with de-wetted surface. Differences in the uptake/leakage rates of compartments have been associated with spontaneous formation of transient nanopores in the membrane under elevated temperatures.[13] The number and size of these pores are random, which can explain the differences in retention of cargo and the comparative rate of loss in structures 6 and 7. Additional patches with and without surface de-wetting were analysed, with the results included in Fig. S3–S8.

Microfluidic device design and process considerations

For open space devices, *i.e.*, microfluidic chips with channel exits at the periphery of the device, the SUEX lamination process has additional challenges. During development of the third (top) lamination layer, viscous resin/developer mixture is drawn into the channels by capillary forces and resides there even after the development process (*cf.* Section S1), which plugs the channel structures at the channel exits. We recently reported a solution that addressed this problem on the wafer scale.[32] However, narrow needle-like outlets can show additional residual SUEX artifacts, originating from the adhesion of the laminate to the wafer close to the chip periphery. Therefore, a narrow gap of 40 μm around the periphery of the entire device was designed into the layers of the wafer design, which (i) prevents unwanted contact of the top laminate layer 3 with the wafer and channel outlets, and (ii) reduces the amount of resin to be developed away to very small amounts. These measures efficiently decreased the amount of photoresist dissolved in the developer during the development process step. This contributed greatly to the prevention of channel exit clogging, completely eliminating resist artifacts at the tip edges (*cf.* Fig. S1).

Benefits of microfluidic superfusion with laminated hard polymer devices

Encapsulation experiments in conjunction with membrane transformations benefit from local stimulation and manipulation of desired regions exclusively within the microscope field of view. Deposition of MLVs on a substrate leads to adhesion and spreading in random areas, which are identified and selected for a given experiment. As in single adherent cell studies, exposing an entire sample with an active solution is unfavourable, since the whole surface population is affected at once. Applying local superfusion with hydrodynamic confinement, the active solution remains in the superfusion zone, and only minute amounts of active solution leave the confinement by diffusion. Multiple experiments can be performed in the same sample preparation: time and cost savings may be tremendous. Most relevant for the current study are the sharp, needle-like tip, overall small footprint and optical transparency of the hard polymer device, which makes deployment and manipulation significantly more convenient, as compared to the soft elastomer microfluidic pipette and the recently presented laminated microdevices. Additionally, the new fabrication route by means of lamination in combination with an optimal wafer layout has led to a rapid, reliable, scalable and fully cleanroom compatible process that can be effortlessly implemented by most laboratories.

Conclusions

The question of retention and fate of fractions of the external volumes, which enters double bilayer pockets during the temperature-induced transformation of flat giant unilamellar vesicles was addressed by means of microfluidic local superfusion. Our findings on the subject reveal that the fractures, which could be observed in some cases to extend from the main patch into the membrane area under the pockets, are open channels through which cargo rapidly escapes into the external volume. The peculiar mechanism, by which the surface is completely de-wetted, where the entire DLB folds and bulges to form a pocket,[10] did not allow us to predict whether the pockets would be completely isolated from the external environment or not. We have now evidence that these pockets are generally leaky, and do not retain the internalized volume. It must be noted that ''conventional'' encapsulation of cargo,

i.e. transport of fluid into the space between distal and proximal bilayer, also occurs on the SiC substrate. In such cases, the pockets are often closed, such that the cargo is maintained in the internal volume on a much longer timescale. Local de-wetting of the proximal bilayer can also occur under such pockets, possibly due to regional differences in adhesion of the DLB to the surface, which differentially de-wet at increased temperatures. We observed that these regions, forming a compartment under the proximal bilayer which is itself enveloped by a distal bilayer superstructure,[13,14] do not retain the cargo material either. It is not clear at this point why these enclosures do not contain fluorescent material. It is possible that there are some pockets of this type that do retain the fluorophores, which would in this case not be visible in the images. Speculatively, the pockets could be filled by drawing fluid from the liquid film between proximal bilayer and surface, which is supported by the observation that these compartments are typically rather small.

The studied membrane transformation on SiC is a process where a completely intact, flat giant unilamellar vesicle (*cf.* patches in Fig. 4B) fragments into smaller, also fully intact daughter vesicles while taking up external content. This can be viewed as a semi-division process combined with encapsulation. Generally, the phenomenon of a surface-adhered compartment fragmenting into smaller, also surface-adhered isolated compartments is an interesting problem for biomechanics, biogenesis of cellular organelles *etc.*, also in the origin of life context as protocell systems forming and transforming autonomously on natural surfaces.

Author contributions

R. L. and R. R. contributed to the design of the study. R. L. developed dry film photolithography method and fabricated microfluidic devices, analysed device parameters. R. R. performed optical microscopy experiments, prepared surfaces, analysed experimental data. R. L. and R. R. designed system components and assembled experimental setup. E. P.-V. substantially assisted with the cleanroom related processes, assisted with the components design, suggested and established the thermal evaporation method. I. G. & A. J. suggested application of the microfluidic device for the investigation of lipid films material retention, designed the experiments, performed data analyses and evaluation, and supervised the project. All authors contributed to the writing of the manuscript.

Conflicts of interest

There are no conflicts of interest to declare.

Data availability

Most of the data supporting this article are included as part of the supplementary information (SI) material. Supplementary information: SI figures and SI video 8 are mentioned in the main manuscript. SI videos 1 and 2 depict solution switching in the microfluidic device and confinement at the tip of the device. SI videos 3–7 provide examples of fluorescent cargo encapsulation. See DOI: https://doi.org/10.1039/d5sm00978b.

Acknowledgements

The authors recognize support given by the engineers of the Microtechnology Centre (MC2). A. J. & R. L. acknowledge "PICK-FOOD" No. 956248 as a funding by the EU's Horizon 2020 research and innovation programme; A. J. & R. R received funding from the EU's Horizon 2020 programme "CREANET" No. 812868. A. J. & E. P.-V. funded by the EU's programme "PROGENY" No. 899205.

References

1 I. Gözen, P. Dommersnes, I. Czolkos, A. Jesorka, T. Lobovkina and O. Orwar, *Nat. Mater.*, 2010, **9**, 908–912.
2 I. Czolkos, A. Jesorka and O. Orwar, *Soft Matter*, 2011, **7**, 4562–4576.
3 S. Joemetsa, K. Spustova, K. Kustanovich, A. Ainla, S. Schindler, S. Eigler, T. Lobovkina, S. Lara-Avila, A. Jesorka and I. Gözen, *Langmuir*, 2019, **35**, 10286–10298.
4 I. Gözen, *ACS Nano*, 2019, **13**, 10869–10871.
5 B. Damer and D. Deamer, *Astrobiology*, 2020, **20**, 429–452.
6 S. Chatterjee and S. Yadav, *Life*, 2022, **12**, 834.
7 N. Stepanyants, H. J. Zhang, T. Lobovkina, P. Dommersnes, G. D. M. Jeffries, A. Jesorka and O. Orwar, *Soft Matter*, 2013, **9**, 5155–5159.
8 H. H. Gerdes, A. Rustom and X. Wang, *Mech. Dev.*, 2013, **130**, 381–387.
9 K. Jahnke, S. J. Maurer, C. Weber, J. E. H. Bücher, A. Schoenit, E. D'Este, E. A. Cavalcanti-Adam and K. Göpfrich, *Nano Lett.*, 2022, **22**, 1145–1150.
10 R. Ryskulov, E. Pedrueza-Villalmanzo, Y. A. Tatli, I. Gözen and A. Jesorka, *EPJ ST*, 2024, **233**, 2743–2756.
11 K. Spustova, L. Xue, R. Ryskulov, A. Jesorka and I. Gözen, *Methods Mol. Biol.*, 2022, **2402**, 209–225.
12 E. S. Köksal, S. Liese, L. Xue, R. Ryskulov, L. Viitala, A. Carlson and I. Gözen, *Small*, 2020, **16**, 2002529.
13 K. Spustova, E. S. Köksal, A. Ainla and I. Gözen, *Small*, 2021, **17**, 2005320.
14 C. Katke, E. Pedrueza-Villalmanzo, K. Spustova, R. Ryskulov, C. N. Kaplan and I. Gözen, *ACS Nano*, 2023, **17**, 3368–3382.
15 R. McCabe and J. Adams, *Dev. Clay Sci.*, 2013, **5**, 491–538.
16 H. J. Cleaves, A. M. Scott, F. C. Hill, J. Leszczynski, N. Sahai and R. Hazen, *Chem. Soc. Rev.*, 2012, **41**, 5502–5525.
17 D. Spitzer, V. Marichez, G. J. M. Formon, P. Besenius and T. M. Hermans, *Angew. Chem., Int. Ed.*, 2018, **57**, 11349–11353.
18 S. H. Liu, P. Gordiichuk, Z. S. Wu, Z. Y. Liu, W. Wei, M. Wagner, N. Mohamed-Noriega, D. Q. Wu, Y. Y. Mai, A. Herrmann, K. Müllen and X. L. Feng, *Nat. Commun.*, 2015, **6**, 8817.
19 T. Bernatowicz, G. Fraundorf, M. Tang, E. Anders, B. Wopenka, E. Zinner and P. Fraundorf, *Nature*, 1987, **330**, 728–730.
20 A. Ainla, E. T. Jansson, N. Stepanyants, O. Orwar and A. Jesorka, *Anal. Chem.*, 2010, **82**, 4529–4536.
21 A. Ainla, S. J. Xu, N. Sanchez, G. D. M. Jeffries and A. Jesorka, *Lab Chip*, 2012, **12**, 4605–4609.

22 A. Ainla, G. D. M. Jeffries, R. Brune, O. Orwar and A. Jesorka, *Lab Chip*, 2012, **12**, 1255–1261.
23 H. J. Zhang, A. Kim, S. J. Xu, G. D. M. Jeffries and A. Jesorka, *Nano Commun. Netw.*, 2015, **6**, 178–182.
24 S. J. Xu, A. Kim, G. D. M. Jeffries and A. Jesorka, *Anal. Bioanal. Chem.*, 2015, **407**, 1295–1301.
25 B. J. Waxse, P. Sengupta, G. G. Hesketh, J. Lippincott-Schwartz and F. Buss, *J. Cell Sci.*, 2017, **130**, 827–840.
26 V. Jové, Z. Y. Gong, F. J. H. Hol, Z. L. Zhao, T. R. Sorrells, T. S. Carroll, M. Prakash, C. S. McBride and L. B. Vosshall, *Neuron*, 2020, **108**, 1163–1180.
27 A. A. Kim, K. Kustanovich, D. Baratian, A. Ainla, M. Shaali, G. D. M. Jeffries and A. Jesorka, *Biomicrofluidics*, 2017, **11**, 014112.
28 S. Farjana, M. Ghaderi, S. Rahiminejad, S. Haasl and P. Enoksson, *Micromachines*, 2021, **12**, 260.
29 N. E. Koucherian, S. J. Yan and E. E. Hui, *Micromachines*, 2022, **13**, 1538.
30 M. M. Roos, A. Winkler, M. Nilsen, S. B. Menzel and S. Strehle, *IJPEM-GT*, 2022, **9**, 43–57.
31 R. Liu, E. Pedrueza-Villalmanzo, F. Fatima and A. Jesorka, *Microfluid. Nanofluid.*, 2025, **29**, 47.
32 R. Liu, E. Pedrueza-Villalmanzo and A. Jesorka, *Sci. Rep.*, 2025, **15**, 32929.
33 I. Gozen, M. Shaali, A. Ainla, B. Ortmen, I. Poldsalu, K. Kustanovich, G. D. Jeffries, Z. Konkoli, P. Dommersnes and A. Jesorka, *Lab Chip*, 2013, **13**, 3822–3826.

